JOURNAL OF GUIDANCE, CONTROL, AND DYNAMICS
Vol. 20, No. 4, July–August 1997

Cycle Ambiguity Estimation for Aircraft Precision Landing Using the Global Positioning System

Boris S. Pervan* and Bradford W. Parkinson†
Stanford University, Stanford, California 94305-4085

Measurements of the Global Positioning System carrier phase can provide the basis for the highest level of satellite-based navigation performance. In particular, the potential exists to exceed even the stringent navigation requirements for aircraft precision approach and landing. The principal difficulty in this use of carrier phase, however, lies in the real-time, high-integrity resolution of the unknown integer cycle ambiguities. A new methodology is introduced, using carrier phase measurements from ground-based pseudolites, for explicit estimation of the cycle ambiguities. The mathematical basis of the new approach is detailed, and high-speed nonlinear information smoothing algorithms suitable for real-time airborne execution are derived. Extensive flight-test data, including the results of automatic landings of a Boeing 737 aircraft, are presented as experimental validation of algorithm performance.

Introduction

THE great potential benefit offered to commercial aviation by the Global Positioning System (GPS) lies in the possibility of inexpensive, seamless navigation from takeoff to touchdown. Although this goal is highly motivating, significant technical challenges have existed, the most difficult of which have been associated with navigation during zero-visibility (Category III) precision landing. The severe requirements for accuracy, integrity, continuity, and availability for this phase of flight are consistent with the use of differential carrier phase, which represents the ultimate realizable GPS navigation performance.

In 1979, Counselman and Shapiro[1] and MacDoran[2] independently extended the existing techniques of very long baseline interferometry to GPS, providing the basis for the use of highly precise differential GPS carrier phase measurements for static survey applications. In 1986, Remondi[3] expanded the concept for application to kinematic survey, and subsequently, differential carrier phase positioning, often called kinematic positioning, has been repeatedly demonstrated to provide the capability for real-time centimeter-level accuracy. This performance has compared favorably in comparison with the traditional meter-level performance associated with the differential use of GPS coarse acquisition (C/A) code phase measurements. However, whereas the C/A code modulation, being expressly designed for the GPS ranging function, provides an absolute range measurement, carrier phase ranging is relative in the sense that an unknown integer bias (cycle ambiguity) exists. As a result, the explicit resolution of these integer cycle ambiguities is required for differential carrier phase positioning.

Existing real-time approaches to cycle ambiguity resolution, based on systematic integer search algorithms (see, for example, Refs. 4 and 5), have been successfully used in a number of applications, including kinematic GPS survey. However, because multiple solutions are fundamentally possible using these techniques, they are inappropriate for high-integrity applications such as aircraft navigation.

Research at Stanford University, supported by the Federal Aviation Administration (FAA), is focused on assessing the feasibility of satellite-based navigation for precision approach and landing. In particular, Stanford's Category III research effort has been centered on combining differential carrier phase measurements with ground-based pseudosatellites (pseudolites) in the development of a navigation system capable of meeting the stringent specifications for precision landing.

The proposed use of ground-based pseudolites for terminal area operations has a historical basis. Klein and Parkinson[6] and Parkinson and Fitzgibbon[7] suggested the use of terminal area GPS pseudolites to improve ranging geometry and, therefore, position accuracy, during precision approach and landing. More recently, Cohen et al.[8] proposed that pseudolites placed under the aircraft approach path could provide the basis for explicit estimation of cycle ambiguities during the approach. Within this context, the present paper is intended to review the underlying theory of cycle ambiguity observability using pseudolites and to provide a rigorous mathematical development of cycle ambiguity estimation algorithms suitable for real-time airborne execution.

Carrier Phase

The carrier phase measured at a GPS receiver is the sum of the true range to the satellite, the cycle ambiguity, and a number of error sources. At an arbitrary epoch k, the carrier phase observable χ_{ik} for spacecraft i can be mathematically expressed as

$$\chi_{ik} = \rho_{ik} + \upsilon_k^R + N_i + \upsilon_{ik}^{sv} - I_{ik} + T_{ik} + \varepsilon_{ik} \tag{1}$$

where

ρ_{ik} = true range between the receiver and satellite i antenna phase centers
υ_k^R = receiver clock offset from nominal GPS time
N_i = integer cycle ambiguity for satellite i
υ_{ik}^{sv} = clock offset of space vehicle (SV) from nominal GPS time, including the effect of selective availability
I_{ik} = carrier phase advance due to the presence of free electrons in the ionosphere along the signal path
T_{ik} = carrier phase delay due to tropospheric refraction
ε_{ik} = sum of multipath (signal reflections received by the antenna) and receiver noise errors

Equation (1) has been nondimensionalized by implicitly expressing time in units of λ/c, where λ is the L1 wavelength (19.03 cm) and c is the vacuum speed of light, and distance in wavelengths λ.

The error effects in the GPS observable are represented by the last four terms in Eq. (1). The effects of receiver noise and multipath will vary depending on the specific antenna and receiver hardware used, the line of sight to the spacecraft, and the localized geography (which is the source of signal reflections). In general, the magnitude of the resulting error is on the order of only a few millimeters. The remaining three error effects, however, can be much larger. These error sources, ionosphere, troposphere, and spacecraft clock (including intentionally induced selective availability errors), can be referenced directly to a given spacecraft's transmission and

Received Aug. 13, 1996; revision received Feb. 21, 1997; accepted for publication Feb. 25, 1997.

*Research Associate, Department of Aeronautics and Astronautics. E-mail: pervan@relgyro.stanford.edu. Member AIAA.
†Professor, Department of Aeronautics and Astronautics. Fellow AIAA.

are independent of the particular user local geography and receiver hardware. In addition, these errors are highly spatially correlated, in the sense that two receivers, e.g., an airborne receiver and ground reference receiver, within a few kilometers of each other will experience essentially identical errors. It is this spatial correlation of errors on which the concept of differential GPS is founded. The basic differential GPS reference station architecture assumed in this research is composed of a GPS receiver, to perform carrier and code phase ranging for all of the satellites in view, and a digital data link, to transmit these measurements to the aircraft for processing.

The single difference phase χ^s_{ik} for satellite i at time k, defined as the difference between airborne (χ^a_{ik}) and reference (χ^r_{ik}) carrier phase measurements, can be expressed as

$$\chi^s_{ik} = \rho^a_{ik} - \rho^r_{ik} + \left(1 - \dot{\chi}^{rs}_{ik}\right)\upsilon_k + N^s_i + v^s_{ik} \tag{2}$$

where the following definitions have been used:

$$\chi^s_{ik} \equiv \chi^a_{ik} - \chi^r_{ik} \tag{3}$$

$$\upsilon_k \equiv \upsilon^a_k - \upsilon^r_k \tag{4}$$

and N^s_i is the difference between aircraft and reference phase cycle ambiguities. The differential clock bias coefficient $\dot{\chi}^{rs}_{ik}$ (the measured reference Doppler) is present to provide the means for implicit time alignment of aircraft and reference measurements, which in practice are generally sampled at different times. This concept is described in more detail in Ref. 9.

The term v^s_{ik} is primarily composed of receiver noise and multipath experienced at both the aircraft and reference receivers but also includes smaller effects associated with the spatial decorrelation of ionospheric, tropospheric, and selective availability errors. The latter contributions will naturally increase in importance as the displacement between the aircraft and reference becomes large.

Differential Satellite Ranging

Because the distance to the satellites is extremely large when compared to the displacement between the reference station and aircraft, the incoming satellite wave fronts are essentially planar (illustrated in Fig. 1). The range difference for satellite i, therefore, can be mathematically expressed as the projection of the displacement vector from the reference to the aircraft $\boldsymbol{x}_k$, onto the line-of-sight (unit) vector to satellite i, $\boldsymbol{e}_{ik}$. Thus, the linearized version of the observation equation (2) is

$$\chi^s_{ik} = -\boldsymbol{e}^\top_{ik}\boldsymbol{x}_k + \left(1 - \dot{\chi}^{rs}_{ik}\right)\upsilon_k + N^s_i + v^s_{ik} \tag{5}$$

The satellite line-of-sight vector $\boldsymbol{e}_{ik}$ is a simple and obvious function of the predicted satellite position (obtained from the broadcast ephemeris) and the approximate user position (which can be easily generated using the differential code-based position).

An example 15-min period of actual single difference phase data is shown in Fig. 2 for one spacecraft. These data were collected across a short baseline (~1 m) on the rooftop of the Hansen Experimental Physics Laboratory (HEPL) at Stanford University using two Trimble Advanced Navigation System (TANS) Quadrex GPS receivers. The apparent linear structure of the single difference phase observable is due to the dominance of the nearly constant drift in the clock bias υ_k (the relative frequency offset from L1) in the receivers.

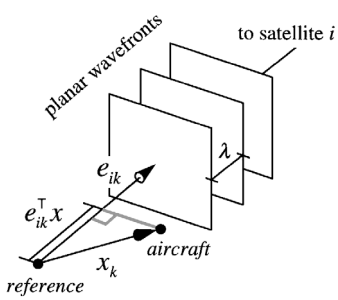

Fig. 1 Planar satellite wave fronts.

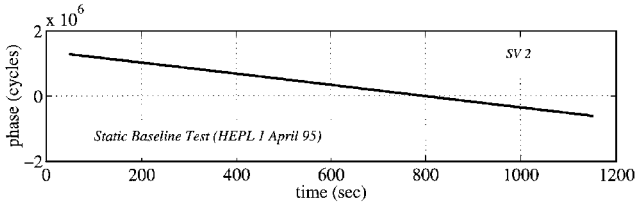

Fig. 2 Single difference phase observable.

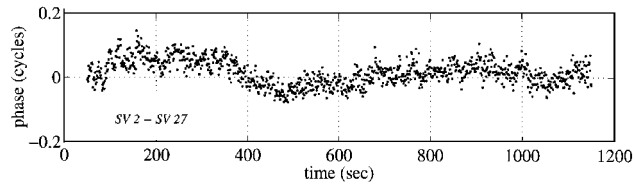

Fig. 3 Double difference phase observable.

This clock bias can be estimated when four or more satellites are in view (as will be discussed shortly) and is not considered a source of error.

To observe the structure of the actual measurement error v^s_{ik}, single difference phase measurements from two satellites can be subtracted from each other to obtain the double difference phase, which effectively serves to remove the common mode clock bias term (see Ref. 9 for more detail). The resulting double difference phase error is shown in Fig. 3. The error structure exhibits both a low-frequency component due to multipath and a white component primarily due to receiver noise. The double difference root-mean-square (rms) error is less than 0.05 cycles (λ), which corresponds to less than 7-mm rms error for the single difference phase error for each independent satellite. The millimeter level precision of carrier phase measurements are readily seen in the results of this simple experiment.

Kinematic Positioning

The carrier phase measurements for n satellites at epoch k can be stacked as follows:

$$\begin{bmatrix} \chi^s_{1k} \\ \vdots \\ \chi^s_{nk} \end{bmatrix} = \begin{bmatrix} -\boldsymbol{e}^\top_{1k} & 1 - \dot{\chi}^{rs}_{1k} \\ \vdots & \vdots \\ -\boldsymbol{e}^\top_{nk} & 1 - \dot{\chi}^{rs}_{nk} \end{bmatrix} \begin{bmatrix} \boldsymbol{x}_k \\ \upsilon_k \end{bmatrix} + \begin{bmatrix} N^s_1 \\ \vdots \\ N^s_n \end{bmatrix} + \begin{bmatrix} v^s_{1k} \\ \vdots \\ v^s_{nk} \end{bmatrix} \tag{6}$$

If the cycle ambiguities are known and $n \geq 4$, it is possible to solve Eq. (6) to obtain the aircraft position relative to the reference station $\boldsymbol{x}_k$. In this event, given the presurveyed location of the reference station with respect to the runway (stored in an aircraft onboard database), centimeter-level position fixes can be forwarded to the aircraft autopilot.

For simplicity of notation, Eq. (6) is rewritten as

$$\phi^s_k = \boldsymbol{H}^s_k \boldsymbol{u}_k + \boldsymbol{N}^s + \boldsymbol{v}^s_k \tag{7}$$

where $\boldsymbol{H}^s_k$ is the $n \times 4$ observation matrix and all other terms are $n \times 1$ vectors. In the general case where a prior estimate of the cycle ambiguity vector $\hat{\boldsymbol{N}}^s$ and its associated covariance $\hat{\boldsymbol{P}}_N$ are available, the least-squares solution to Eq. (7) is

$$\hat{\boldsymbol{u}}_k = \left(\boldsymbol{H}^{s\top}_k \boldsymbol{V}^{-1}_s \boldsymbol{H}^s_k\right)^{-1} \boldsymbol{H}^{s\top}_k \boldsymbol{V}^{-1}_s \left(\phi^s_k - \hat{\boldsymbol{N}}^s\right) \tag{8}$$

The weighting matrix

$$\boldsymbol{V}_s \equiv \hat{\boldsymbol{P}}^s_N + \boldsymbol{I}_n \sigma^2_\chi \tag{9}$$

is the sum of the cycle ambiguity error covariance matrix and the measurement error covariance matrix. The form of the latter matrix implicitly assumes independent, identically distributed measurements with variance σ^2_χ. If $\hat{\boldsymbol{N}}^s$ is an unbiased estimate of $\boldsymbol{N}^s$ and all errors are normally distributed, Eq. (8) provides an unbiased, maximum likelihood estimate of $\boldsymbol{u}_k$.

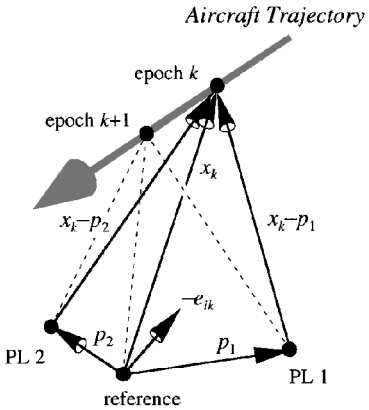

Fig. 4 Pseudolite geometry.

The estimate error covariance is given by

$$\hat{\boldsymbol{P}}_u = E\left[(\boldsymbol{u}_k - \hat{\boldsymbol{u}}_k)(\boldsymbol{u}_k - \hat{\boldsymbol{u}}_k)^\top\right] = \left(\boldsymbol{H}_k^{s\top}\boldsymbol{V}_s^{-1}\boldsymbol{H}_k^s\right)^{-1} \tag{10}$$

Relations (9) and (10) express the quality of the position and clock estimate $\hat{\boldsymbol{u}}_k$ in terms of how well the cycle ambiguities are known ($\hat{\boldsymbol{P}}_N$), the precision of the carrier phase measurements (σ_χ), and the quality of the particular spacecraft geometry ($\boldsymbol{H}_k^s$).

Differential Pseudolite Ranging

Anticipating the application of ground-based pseudolites in the near vicinity of the aircraft and reference station (Fig. 4), linearity of pseudolite wave fronts cannot be assumed. The single difference observable for pseudolite i must instead be expressed in discrete-time form by

$$\chi_{ik}^p = |\boldsymbol{p}_i - \boldsymbol{x}_k| + \left(1 - \dot{\chi}_{ik}^{rp}\right)\upsilon_k + N_i^p + v_{ik}^p \tag{11}$$

where $\boldsymbol{p}_i$ is the baseline vector from the reference station antenna to the transmit antenna of pseudolite i. Once the ground segment is installed, this baseline vector can be obtained to millimeter-level accuracy using well-established GPS static survey techniques. The constant N_i^p differs in character from its spacecraft counterpart N_i^s by the addition of a bias associated with the transmission of the pseudolite signal to the reference station via coaxial cable. In general, N_i^p will not be an integer.

Cycle Ambiguity Resolution and Pseudolites

Satellite motion, together with redundant measurements, can provide the observability for direct estimation of the integer cycle ambiguities. This approach is ideally suited for GPS applications in which time is not a significant constraint; in fact, most GPS static survey systems are founded on this principle. Additionally, the use of redundant measurements for explicit motion-based estimation can ensure the integrity of cycle ambiguity resolution. This property, discussed in Ref. 9, makes motion-based estimation highly attractive for precision approach and landing applications. Unfortunately, the rate of satellite motion is very slow in comparison with the time scales of most real-time applications, including precision approach and landing. As a result, satellite motion alone can provide only marginal leverage for real-time cycle ambiguity estimation.[10,11] In addition, five or more satellites are needed for direct estimation in nonstatic situations; thus, the availability of satellite-motion-based resolution is limited.

The introduction of ground-based pseudolites can provide the advantages and alleviate the disadvantages of motion-based cycle ambiguity resolution. If the pseudolites are placed under the aircraft approach path, the large geometry change that occurs during aircraft overflight can provide, on a time scale of a few seconds, the observability needed for explicit cycle ambiguity resolution. Furthermore, if pseudolites are implemented, redundant satellites are not needed; thus, availability is ensured.

Absolute Position Observability

The geometric basis for cycle ambiguity resolution using ground-based pseudolites can be explained in relatively simple mathematical terms. For clarity of explanation, the (scalar) pseudolite and (vector) satellite single difference phase observables [Eqs. (7) and (11)] are simplified as

$$\chi_k^p = |\boldsymbol{x}_k| + \upsilon_k + N^p \tag{12}$$

$$\phi_k^s = \boldsymbol{H}^s\begin{bmatrix}\boldsymbol{x}_k\\ \upsilon_k\end{bmatrix} + \boldsymbol{N}^s \tag{13}$$

where spacecraft motion during pseudolite overflight, time alignment terms, and measurement error have been ignored. These neglected effects are irrelevant to the present observability discussion. In addition, a single pseudolite located at $\boldsymbol{p}_1 = 0$ (the reference site) has been assumed.

Differencing the satellite phase at epoch k in Eq. (13) from the phase at epoch 0 (the first epoch during pseudolite overflight) and inverting, the following relation is easily obtained:

$$\begin{bmatrix}\boldsymbol{x}_{k-0}\\ \upsilon_{k-0}\end{bmatrix} \equiv \begin{bmatrix}\boldsymbol{x}_k - \boldsymbol{x}_0\\ \upsilon_k - \upsilon_0\end{bmatrix} = \boldsymbol{H}^{s^{-1}}\phi_{k-0}^s \tag{14}$$

where it has been assumed that four satellites are used so that $\boldsymbol{H}^s$ is invertible. The terms $\boldsymbol{x}_{k-0}$ and υ_{k-0} describe the relative trajectory and clock that are available from satellite ranging alone. Substituting these terms into the pseudolite observation equation (12) and collecting bias terms into a single constant b, the following expression is obtained:

$$\chi_k^p = |\boldsymbol{x}_{k-0} + \boldsymbol{x}_0| + \upsilon_{k-0} + b \tag{15}$$

The initial position $\boldsymbol{x}_0$ and bias b are now the only variables on the right-hand side of Eq. (15), and the variation in the pseudolite phase profile with respect to these parameters is given to first order by

$$\delta\chi_k^p = \left(\boldsymbol{x}_k^\top / |\boldsymbol{x}_k|\right)\delta\boldsymbol{x}_0 + \delta b \tag{16}$$

Consider now the idealized linear pseudolite overflight trajectory shown in Fig. 5 in which the radial (vertical) component of absolute position is constant and the crosstrack component is identically zero. In this case, Eq. (16) becomes

$$\delta\chi_k^p = \begin{bmatrix}\dfrac{x_k^i}{|\boldsymbol{x}_k|} & 0 & \dfrac{x_0^r}{|\boldsymbol{x}_k|} & 1\end{bmatrix}\begin{bmatrix}\delta x_0^i\\ \delta x_0^c\\ \delta x_0^r\\ \delta b\end{bmatrix} \tag{17}$$

The basis functions for intrack ($x_k^i/|\boldsymbol{x}_k|$) and radial ($x_0^r/|\boldsymbol{x}_k|$) absolute position are expressed graphically in Fig. 6 vs intrack position (normalized by x_0^r). Figure 6 shows that the effects on the pseudolite phase profile of radial and intrack absolute position deviations

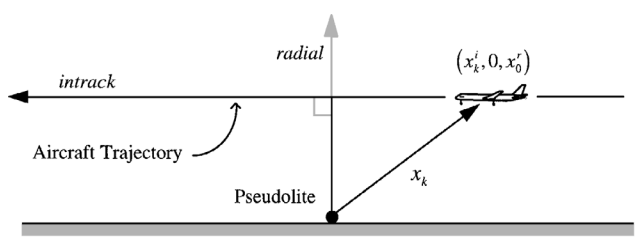

Fig. 5 Pseudolite overflight geometry.

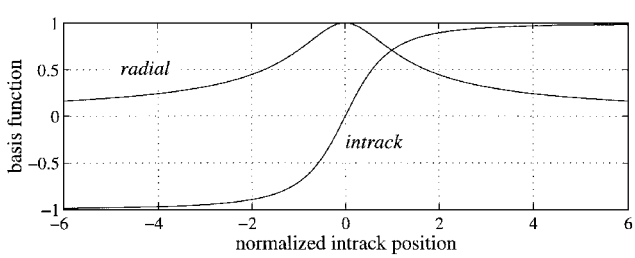

Fig. 6 Absolute position basis functions.

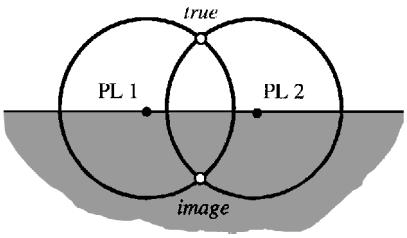

Fig. 7 Contours of absolute position: intrack view.

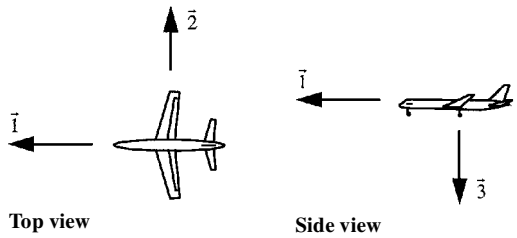

Fig. 8 Aircraft body axes.

are clearly distinguishable from each other and from the bias in Eq. (17) provided that there is a reasonably large relative geometry change, as determined by the normalized intrack position history. However, it is also clear from Eq. (17) that no information is present in the pseudolite phase profile concerning deviations in crosstrack absolute position. In fact, all trajectories consistent with the relative position history [Eq. (14)] that have an initial intrack position of x_0^i and lie on the surface of a cylinder with radius x_0^r (with central axis along the ground track) will also be consistent with the collected pseudolite phase measurements.

The introduction of a second pseudolite, however, provides the means for full three-dimensional absolute positioning. Figure 7 shows an intrack view of the cylinders of absolute position (represented by the circular contours) using two pseudolites. For the idealized linear trajectory just described, the contours of absolute position intersect at two points: the true solution and an image solution. In reality, because the image solution is underground, it can be easily rejected as false. Furthermore, it will be shortly demonstrated that, given even relatively poor initial knowledge of the aircraft position, convergence to the true solution can be ensured.

Cycle Ambiguity Observability

In practice, the information collected from the satellites and pseudolites during pseudolite overflight is processed to obtain cycle ambiguity estimates $\hat{\boldsymbol{N}}^s$ and estimate-error covariance matrix $\hat{\boldsymbol{P}}_N^s$ for all spacecraft in view. These, in turn, are substituted into Eqs. (8) and (9) to provide absolute kinematic position fixes at any epoch after pseudolite overflight.

Within this context, the issue of cycle ambiguity observability must be addressed. Specifically, the single difference observation equations (5) and (11) contain both the cycle ambiguities (N_i^s and N_i^p) and a clock bias term (υ_k). Because the coefficients of the clock bias, $1-\dot{\phi}_{ik}^{rs}$ and $1-\dot{\phi}_{ik}^{rp}$, are always nearly unity and the clock bias is common to all ranging measurements, it is essentially impossible to distinguish the integer cycle ambiguity for a given channel from the clock bias. Fortunately, this is not required. To resolve this issue, Eqs. (5) and (11) are rewritten in terms of cycle ambiguity differences for the n_s satellite measurements and n_p pseudolite measurements as follows:

$$\chi_{1k}^s = -\boldsymbol{e}_{1k}^\top \boldsymbol{x}_k + \left(1-\dot{\chi}_{1k}^{rs}\right)\left(\upsilon_k + N_1^s\right) + \dot{\chi}_{1k}^r N_1^s + v_{1k}^s \tag{18}$$

$$\chi_{ik}^s = -\boldsymbol{e}_{ik}^\top \boldsymbol{x}_k + \left(1-\dot{\chi}_{ik}^{rs}\right)\left(\upsilon_k + N_1^s\right) + \left(N_i^s - N_1^s\right) + \dot{\chi}_{ik}^r N_1^s + v_{ik}^s \qquad (i=2,n_s) \tag{19}$$

$$\chi_{ik}^p = |\boldsymbol{p}_i - \boldsymbol{x}_k| + \left(1-\dot{\chi}_{ik}^{rp}\right)\left(\upsilon_k + N_1^s\right) + \left(N_i^p - N_1^s\right) + \dot{\chi}_{ik}^r N_1^s + v_{ik}^p \qquad (i=1,n_p) \tag{20}$$

cycles, all products of the form $\dot{\phi}_{ik}^r N_1^s$ in Eqs. (18–20) are less than 0.2 mm and can be neglected. This condition is easily satisfied if an initial differential code phase measurement for satellite 1 is used to obtain an estimate of this cycle ambiguity, and then this estimate is subtracted from all subsequent carrier phase measurements for satellite 1. Consequently, Eqs. (18–20) can be simplified as

$$\chi_{1k}^s = -\boldsymbol{e}_{1k}^\top \boldsymbol{x}_k + \left(1-\dot{\chi}_{1k}^{rs}\right)\upsilon_k^1 + v_{1k}^s \quad \text{(master satellite)} \tag{21}$$

$$\chi_{ik}^s = -\boldsymbol{e}_{ik}^\top \boldsymbol{x}_k + \left(1-\dot{\chi}_{1k}^{rs}\right)\upsilon_k^1 + \Delta N_i^s + v_{ik}^s \qquad (i=2,n_s) \tag{22}$$

$$\chi_{ik}^p = |\boldsymbol{p}_i - \boldsymbol{x}_k| + \left(1-\dot{\chi}_{ik}^{rp}\right)\upsilon_k^1 + \Delta N_i^p + v_{ik}^p \qquad (i=1,n_p) \tag{23}$$

where the following definitions have been made:

$$\upsilon_k^1 \equiv \upsilon_k + N_1^s \tag{24}$$

$$\Delta N_i^s \equiv N_i^s - N_1^s \tag{25}$$

$$\Delta N_i^p \equiv N_i^p - N_1^s \tag{26}$$

The observation equations (21–23) will be used as the basis for the development of cycle ambiguity resolution algorithms in the following sections.

Attitude and Moment Arm

An additional practical issue, which must be addressed, is the fact that the satellite signals are tracked via an antenna mounted on top of the aircraft fuselage, whereas the pseudolite signals must be received through an antenna mounted on the belly of the fuselage. Specifically, if $\boldsymbol{x}_k$ is defined to be the displacement vector from the reference station antenna to the aircraft top antenna at epoch k, then Eq. (23) must be more precisely expressed for $(i=1,n_p)$ as

$$\chi_{ik}^p = |\boldsymbol{p}_i - (\boldsymbol{x}_k + \boldsymbol{\ell}_k)| + \left(1-\dot{\chi}_{ik}^{rp}\right)\upsilon_k^1 + \Delta N_i^p + v_{ik}^p \tag{27}$$

where $\boldsymbol{\ell}_k$ is the moment arm vector from the top antenna to the belly antenna. When $\boldsymbol{x}_k$ is expressed in local reference coordinates (for example, east, north, and up), then the moment arm will necessarily be a function of aircraft attitude.

Given a one-time preflight calibration of the moment arm $\boldsymbol{\ell}^b$, expressed in aircraft body axes (Fig. 8), and an aircraft orientation expressed as a rotation ψ in azimuth (from north), followed by a pitch of θ from the local horizontal and roll angle φ, Eq. (27) can be rewritten as

$$\chi_{ik}^p = \left|\boldsymbol{p}_i - \left(\boldsymbol{x}_k + \boldsymbol{A}_k \boldsymbol{\ell}^b\right)\right| + \left(1-\dot{\chi}_{ik}^{rs}\right)\upsilon_k^1 + \Delta N_i^p + v_{ik}^p \qquad (i=1,n_p) \tag{28}$$

where the rotation matrix A_k is defined as

$$\boldsymbol{A}_k \equiv \begin{bmatrix} \cos\theta\sin\psi & \cos\varphi\cos\psi + \sin\varphi\sin\theta\sin\psi & -\sin\varphi\cos\psi + \cos\varphi\sin\theta\sin\psi \\ \cos\theta\cos\psi & -\cos\varphi\sin\psi + \sin\varphi\sin\theta\cos\psi & \sin\varphi\sin\psi + \cos\varphi\sin\theta\cos\psi \\ \sin\theta & -\sin\varphi\cos\theta & -\cos\varphi\cos\theta \end{bmatrix}_k \tag{29}$$

For simplicity, the integer for satellite 1 has been chosen as master for differencing; however, the choice of master satellite is arbitrary and does not in any way affect absolute positioning. If $N_1^s < 200$

This same procedure can also be used to translate the fuselage top antenna position to an appropriate autopilot reference point such as the aircraft landing gear.

Mathematics of Cycle Ambiguity Resolution

Least-squares estimation of cycle ambiguities involves the processing of pseudolite measurements (28), which are nonlinear in the aircraft position. The development of cycle ambiguity estimation algorithms to process these measurements is driven by the high-speed and high-integrity needs of the envisioned real-time airborne application.

Batch Algorithms

The resolution of cycle ambiguities by means of a Gauss–Newton batch algorithm requires the linearization of the pseudolite observation equation about the best current trajectory estimate. Given an approximate initial trajectory $\bar{\boldsymbol{x}}_k$ obtained from code-based differential GPS (DGPS) the pseudolite observation equation (28) can be expressed in terms of the deviation from the approximate trajectory: $\delta\boldsymbol{x}_k \equiv \boldsymbol{x}_k - \bar{\boldsymbol{x}}_k$. Keeping first-order terms only, the result is as follows:

$$\delta\chi^p_{ik} \equiv \chi^p_{ik} - \left|\boldsymbol{p}_i - \left(\bar{\boldsymbol{x}}^i_k + \boldsymbol{A}_k\boldsymbol{\ell}^b\right)\right| = -\bar{\boldsymbol{e}}^\top_{ik}\delta\boldsymbol{x}_k + \left(1 - \dot{\chi}^{rp}_{ik}\right)\upsilon^1_k + \Delta N^p_i + v^p_{ik} \qquad (i = 1, n_p) \quad (30)$$

where

$$\bar{\boldsymbol{e}}^\top_{ik} \equiv \frac{\left[\boldsymbol{p}_i - \left(\bar{\boldsymbol{x}}^i_k + \boldsymbol{A}_k\boldsymbol{\ell}^b\right)\right]^\top}{\left|\boldsymbol{p}_i - \left(\bar{\boldsymbol{x}}^i_k + \boldsymbol{A}_k\boldsymbol{\ell}^b\right)\right|} \quad (31)$$

is the approximate line-of-sight vector at epoch k from the aircraft top antenna to pseudolite i. For consistency, the satellite observations are also expressed in terms of the deviation from the approximate trajectory as follows:

$$\delta\chi^s_{1k} \equiv \chi^s_{1k} + \boldsymbol{e}^\top_{1k}\bar{\boldsymbol{x}}_k = -\boldsymbol{e}^\top_{1k}\delta\boldsymbol{x}_k + \left(1 - \dot{\chi}^{rs}_{1k}\right)\upsilon^1_k + v^s_{1k} \quad (32)$$

$$\delta\chi^s_{ik} \equiv \chi^s_{ik} + \boldsymbol{e}^\top_{ik}\bar{\boldsymbol{x}}_k = -\boldsymbol{e}^\top_{ik}\delta\boldsymbol{x}_k + \left(1 - \dot{\chi}^{rs}_{ik}\right)\upsilon^1_k + \Delta N^s_i + v^s_{ik} \qquad (i = 2, n_s) \quad (33)$$

Defining $\delta\phi_k$ to be the vector of n_s satellite and n_p pseudolite measurements at epoch k as

$$\delta\phi_k \equiv \begin{bmatrix} \delta\chi^s_{1k} \\ \vdots \\ \delta\chi^s_{n_sk} \\ \delta\chi^p_{1k} \\ \vdots \\ \delta\chi^p_{n_pk} \end{bmatrix} \quad (34)$$

and $\boldsymbol{E}_k$, the observation matrix at epoch k, as

$$\boldsymbol{E}_k \equiv \begin{bmatrix} -\boldsymbol{e}^\top_{1k} & 1 - \dot{\chi}^{rs}_{1k} \\ \vdots & \vdots \\ -\boldsymbol{e}^\top_{n_sk} & 1 - \dot{\chi}^{rs}_{n_sk} \\ -\bar{\boldsymbol{e}}^\top_{1k} & 1 - \dot{\chi}^{rp}_{1k} \\ \vdots & \vdots \\ -\bar{\boldsymbol{e}}^\top_{n_pk} & 1 - \dot{\chi}^{rp}_{n_pk} \end{bmatrix} \quad (35)$$

and stacking the measurements obtained at the n epochs inside the pseudolite bubble (where the bubble is defined as the volume within which the pseudolite signal is trackable by the airborne receiver), the following matrix equation results:

$$\begin{bmatrix} \delta\phi_1 \\ \vdots \\ \delta\phi_k \\ \vdots \\ \delta\phi_n \end{bmatrix} = \begin{bmatrix} \boldsymbol{E}_1 & \boldsymbol{0} & \cdots & \boldsymbol{0} & \boldsymbol{0} & \bar{\boldsymbol{I}} \\ \boldsymbol{0} & \ddots & \boldsymbol{0} & \ddots & \boldsymbol{0} & \vdots \\ \vdots & \ddots & \boldsymbol{E}_k & \ddots & \vdots & \bar{\boldsymbol{I}} \\ \boldsymbol{0} & \ddots & \boldsymbol{0} & \ddots & \boldsymbol{0} & \vdots \\ \boldsymbol{0} & \boldsymbol{0} & \cdots & \boldsymbol{0} & \boldsymbol{E}_n & \bar{\boldsymbol{I}} \end{bmatrix} \begin{bmatrix} \delta\boldsymbol{u}_1 \\ \vdots \\ \delta\boldsymbol{u}_k \\ \vdots \\ \delta\boldsymbol{u}_n \\ \boldsymbol{N} \end{bmatrix} + \boldsymbol{v} \quad (36)$$

where the following definitions have been assumed:

$$\bar{\boldsymbol{I}} \equiv \begin{bmatrix} \boldsymbol{0}^\top \\ \boldsymbol{I} \end{bmatrix} \quad (37)$$

$$\delta\boldsymbol{u}_k \equiv \begin{bmatrix} \delta\boldsymbol{x}_k \\ \upsilon^1_k \end{bmatrix} \quad (38)$$

$$\boldsymbol{N} \equiv \begin{bmatrix} \Delta N^s_2 \\ \vdots \\ \Delta N^s_{n_s} \\ \Delta N^p_1 \\ \vdots \\ \Delta N^p_{n_p} \end{bmatrix} \quad (39)$$

and $\boldsymbol{0}$ in relation (37) is the null vector of length $n_s + n_p - 1$.

The linear least-squares solution to Eq. (36) is obtained and the resulting estimate of the trajectory deviation $\delta\hat{\boldsymbol{x}}_k$ is used to adjust the approximate trajectory: $\bar{\boldsymbol{x}}^{\text{new}}_k = \bar{\boldsymbol{x}}^{\text{old}}_k + \delta\hat{\boldsymbol{x}}_k$. This process, generally known as Gauss–Newton iteration, is repeated using the new trajectory and is continued through convergence.

In practice, the difficulty with the straightforward application of this procedure is due to the large size of the observation matrix in Eq. (36), which when $n = 50$ can exceed 500×200, requiring nearly 1 Mbyte of memory to store. More importantly, the total computation time for such a problem can surpass 60 s on a Pentium computer. These difficulties, in particular the long computation time, prohibit the direct application of the simple batch least-squares algorithm just outlined and establish the need for the development of new, efficient, high-speed algorithms for nonlinear least-squares estimation.

The sparse nature of the observation matrix in Eq. (36) can provide the basis for the needed improvements in both execution time and storage efficiency. However, sparse matrix batch algorithms are relatively inflexible to certain conditions seen in practical airborne applications. Specifically, consider the situation where the GPS receiver loses phase lock on a previously tracked satellite or pseudolite or acquires a new satellite or pseudolite while the algorithm is in the process of stacking phase data for batch processing. These events are, in fact, very common in practice, especially for low-elevation satellites and for pseudolites when the aircraft is near the bubble boundary. The inherently rigid structure of batch least-squares algorithms, however, makes accounting for these events very difficult in that a given satellite or pseudolite may occasionally have two or more cycle ambiguities that need to be resolved, only one of which will actually be applicable after bubble exit. Thus, further motivation is provided for the development of algorithms that provide the least-squares solution to Eq. (36) and retain the high-speed characteristics of sparse matrix algorithms but are more adaptable to the conditions present in real-time airborne applications. These objectives can be met by a reformulation of the problem within the context of sequential information smoothing.[12]

Iterated Information Smoother

At any epoch k within the pseudolite bubble, the vector of satellite and pseudolite measurements can be written in vector form as

$$\delta\phi_k = \begin{bmatrix} \boldsymbol{E}_k & \bar{\boldsymbol{I}} \end{bmatrix} \begin{bmatrix} \delta\boldsymbol{u}_k \\ \boldsymbol{N} \end{bmatrix} + \boldsymbol{v}_k \quad (40)$$

where the measurement noise vector $\boldsymbol{v}_k$ is distributed as $\boldsymbol{v}_k \sim N(\boldsymbol{0}, \sigma^2_\chi \boldsymbol{I}_{n_s+n_p})$ and the other variables in Eq. (40) are as previously defined. If no satellites or pseudolites are lost or acquired between epochs k and $k+1$, the aircraft kinematics can be expressed as a discrete Gauss–Markov process as follows:

$$\begin{bmatrix} \delta\boldsymbol{u} \\ \boldsymbol{N} \end{bmatrix}_{k+1} = \begin{bmatrix} \delta\boldsymbol{u} \\ \boldsymbol{N} \end{bmatrix}_k + \boldsymbol{w}_k \quad (41)$$

where the process noise vector $\boldsymbol{w}_k$ is distributed as $\boldsymbol{w}_k \sim N(\boldsymbol{0}, \boldsymbol{W})$ and

$$\boldsymbol{W} \equiv \lim_{\mu \to \infty} \begin{bmatrix} \mu \boldsymbol{I}_4 & \boldsymbol{0} \\ \boldsymbol{0} & \boldsymbol{0} \end{bmatrix} \tag{42}$$

The process noise covariance matrix $\boldsymbol{W}$ effectively invokes infinite process noise on the vehicle position and clock states in order to emulate the purely kinematic structure of Eq. (36) and zero process noise on the cycle ambiguities, which are, of course, constant in time.

Given a state estimate-error covariance $\hat{\boldsymbol{P}}_{k-1}$, the covariance time update $\bar{\boldsymbol{P}}_k$ based on Eqs. (41) and (42) is

$$\bar{\boldsymbol{P}}_k = \hat{\boldsymbol{P}}_{k-1} + \boldsymbol{W} = \lim_{\mu \to \infty} \begin{bmatrix} \mu \boldsymbol{I}_4 & \hat{\boldsymbol{P}}_{uN} \\ \hat{\boldsymbol{P}}_{uN}^{\top} & \hat{\boldsymbol{P}}_N \end{bmatrix}_{k-1} \tag{43}$$

where $\hat{\boldsymbol{P}}_{uN}$, $4 \times (n_s + n_p - 1)$, and $\hat{\boldsymbol{P}}_N$, $(n_s + n_p - 1) \times (n_s + n_p - 1)$, are the right upper and lower subblocks of $\hat{\boldsymbol{P}}$. This result can also be expressed in information matrix form as

$$\bar{\boldsymbol{S}}_k = \begin{bmatrix} \boldsymbol{0} & \boldsymbol{0} \\ \boldsymbol{0} & \hat{\boldsymbol{P}}_N^{-1} \end{bmatrix}_{k-1} \tag{44}$$

where $\hat{\boldsymbol{P}}_N^{-1}$ is the inverse of the lower right block of $\hat{\boldsymbol{P}}$ that corresponds to the integer states. The information matrix measurement update can then be applied to obtain

$$\hat{\boldsymbol{S}}_k = \begin{bmatrix} \boldsymbol{0} & \boldsymbol{0} \\ \boldsymbol{0} & \hat{\boldsymbol{P}}_N^{-1} \end{bmatrix}_{k-1} + \begin{bmatrix} \boldsymbol{E}_k^{\top} \\ \bar{\boldsymbol{I}}^{\top} \end{bmatrix} [\boldsymbol{E}_k \quad \bar{\boldsymbol{I}}] \tag{45}$$

where, for clarity, the measurement covariance has been normalized by σ_χ^2. Using familiar matrix block inversion identities, Eq. (45) can be written explicitly in information form as follows:

$$\hat{\boldsymbol{S}}_k = \begin{bmatrix} \boldsymbol{0} & \boldsymbol{0} \\ \boldsymbol{0} & \hat{\boldsymbol{S}}_N - \hat{\boldsymbol{S}}_{uN}^{\top} \hat{\boldsymbol{S}}_u^{-1} \hat{\boldsymbol{S}}_{uN} \end{bmatrix}_{k-1} + \begin{bmatrix} \boldsymbol{E}_k^{\top} \\ \bar{\boldsymbol{I}}^{\top} \end{bmatrix} [\boldsymbol{E}_k \quad \bar{\boldsymbol{I}}] \tag{46}$$

where the matrix $\hat{\boldsymbol{S}}_u$, the upper left 4×4 block of the information matrix, is full rank at epoch k if four or more measurements (satellite and pseudolite) are available. For GPS positioning to be possible in any form, this condition must always be satisfied.

Defining the information vector as

$$\boldsymbol{y}_k \equiv \begin{bmatrix} \boldsymbol{y}_u \\ \boldsymbol{y}_N \end{bmatrix}_k \equiv \boldsymbol{S}_k \begin{bmatrix} \delta \boldsymbol{u} \\ \boldsymbol{N} \end{bmatrix}_k \tag{47}$$

where $\boldsymbol{y}_u$ is 4×1 and $\boldsymbol{y}_N$ is $(n_s + n_p - 1) \times 1$, the state update can be shown through a similar derivation to be given by

$$\hat{\boldsymbol{y}}_k = \begin{bmatrix} \boldsymbol{0} \\ \hat{\boldsymbol{y}}_N - \hat{\boldsymbol{S}}_{uN}^{\top} \hat{\boldsymbol{S}}_u^{-1} \hat{\boldsymbol{y}}_u \end{bmatrix}_{k-1} + \begin{bmatrix} \boldsymbol{E}_k^{\top} \\ \bar{\boldsymbol{I}}^{\top} \end{bmatrix} \delta \phi_k \tag{48}$$

Under nominal circumstances, when satellites and pseudolites are not lost or acquired during the bubble pass, Eqs. (46) and (48) can be applied sequentially, without modification (with initial conditions $\bar{\boldsymbol{y}}_1 = \boldsymbol{0}$ and $\bar{\boldsymbol{S}}_1 = \boldsymbol{0}$), until the final bubble epoch n is reached. At this point, the information matrix $\hat{\boldsymbol{S}}_n$ is invertible and cycle ambiguity estimates may be computed using Eq. (47). However, to ensure a solution consistent with a Gauss–Newton solution to Eq. (36), an updated trajectory must be obtained and the process must be repeated through convergence. To obtain an identical updated trajectory to that provided by the batch solution to Eq. (36), backward smoothing of the collected measurements is necessary. This is easily done by interchanging the k and $k-1$ indices in Eqs. (46) and (48) and regressing sequentially through the data with the initial conditions $\bar{\boldsymbol{y}}_n$ and $\bar{\boldsymbol{S}}_n = \boldsymbol{0}$. The information vector and matrix obtained from backward processing are added to the stored results from the forward pass according to

$$\hat{\boldsymbol{S}}_k = \hat{\boldsymbol{S}}_k^F + \bar{\boldsymbol{S}}_k^B \tag{49}$$

$$\hat{\boldsymbol{y}}_k = \hat{\boldsymbol{y}}_k^F + \bar{\boldsymbol{y}}_k^B \tag{50}$$

The trajectory update $\delta \hat{\boldsymbol{x}}_k$ can now be realized as a vector element of $\hat{\boldsymbol{S}}_k^{-1} \hat{\boldsymbol{y}}_k$. The entire process is then repeated until $\delta \hat{\boldsymbol{x}}_k$ is negligibly small.

One utility of the information smoother algorithm is that, like the batch formulation of Eq. (36), no prior information is needed to begin. Not surprisingly, this property is also useful when new satellites or pseudolites are acquired or lost during stacking and processing. These events are accommodated in a relatively straightforward manner using the matrix block inversion methods described in the Appendix.

Furthermore, due to the efficient and compact structure inherent in sequential least-squares processing, the iterated information smoother retains the high-speed characteristics of the sparse matrix batch solution; for a stack size of $n = 50$, execution time on a Pentium processor is typically 1–1.5 s.

Reduced-Order Iterated Information Smoother

It is possible to further increase speed of execution through the application of a reduced-order smoother formulation. The central assumption underlying this approach is that the satellite measurements provide information regarding the relative kinematic trajectory only, while the pseudolite measurements provide the means for absolute placement (in the local airport reference frame) of this relative trajectory. This notion is essentially identical to that used in the observability analysis covered earlier. In the strictest sense, however, the cycle ambiguity estimates that result from this approach will be approximate because they are not obtained from the least-squares solution to the system of equations (36). Nevertheless, the underlying assumptions are not unrealistic and, thus, the improvement in speed afforded by the reduced-order algorithm motivates its further development.

The vector of satellite phase measurements at epoch k can be expressed as

$$\delta \phi_k^s = \boldsymbol{E}_k^s \delta \boldsymbol{u}_k + \begin{bmatrix} 0 \\ \Delta N_2^s \\ \vdots \\ \Delta N_{n_s}^s \end{bmatrix} + \boldsymbol{v}_k^s \tag{51}$$

Similarly, the pseudolite phase measurements can be written as

$$\delta \phi_k^p = \boldsymbol{E}_k^p \delta \boldsymbol{u}_k + \begin{bmatrix} \Delta N_1^p \\ \vdots \\ \Delta N_{n_p}^p \end{bmatrix} + \boldsymbol{v}_k^p \tag{52}$$

Subtracting the integer vector from both sides of Eq. (51), solving for $\delta \boldsymbol{u}_k$, and substituting the result into Eq. (52) yields

$$\delta \phi_k^p - \boldsymbol{E}_k^p \boldsymbol{E}_k^{s+} \delta \phi_k^s = \begin{bmatrix} -\boldsymbol{E}_k^p \boldsymbol{E}_k^{s+} & \boldsymbol{I}_{n_p} \end{bmatrix} \begin{bmatrix} 0 \\ \boldsymbol{N} \end{bmatrix} - \boldsymbol{E}_k^p \boldsymbol{E}_k^{s+} \boldsymbol{v}_k^s + \boldsymbol{v}_k^p \tag{53}$$

where $\boldsymbol{N}$ is defined in Eq. (39) and

$$\boldsymbol{E}_k^{s+} \equiv \left(\boldsymbol{E}_k^{s\top} \boldsymbol{E}_k^s \right)^{-1} \boldsymbol{E}_k^{s\top} \tag{54}$$

The reduced-order observation equation (53) can be written in compact form as

$$\delta \phi_k^R = \boldsymbol{E}_k^R \boldsymbol{N} + \boldsymbol{v}_k^R \tag{55}$$

where $\boldsymbol{E}_k^R$ is the observation matrix in Eq. (53) with the first column removed, and the error vector is distributed as

$$\boldsymbol{v}_k^R \sim N(\boldsymbol{0}, \boldsymbol{V}_k), \qquad \boldsymbol{V}_k \equiv \sigma_\chi^2 \left[\boldsymbol{I}_{n_p} + \boldsymbol{E}_k^p \left(\boldsymbol{E}_k^{s\top} \boldsymbol{E}_k^s \right)^{-1} \boldsymbol{E}_k^{p\top} \right] \tag{56}$$

The stack of measurements [Eq. (55)] collected over n epochs in the pseudolite bubble can be processed using sequential static least

squares. Because no prior information on the integer state vector $\boldsymbol{N}$ is assumed, the following information algorithm is used:

$$\hat{\boldsymbol{S}}_n^N = \sum_{k=1}^{n} \boldsymbol{E}_k^{R\top} \boldsymbol{V}_k^{-1} \boldsymbol{E}_k^R \tag{57}$$

$$\hat{\boldsymbol{y}}_n^N = \sum_{k=1}^{n} \boldsymbol{E}_k^{R\top} \boldsymbol{V}_k^{-1} \delta\phi_k^R \tag{58}$$

where $[\hat{\boldsymbol{S}}_k^N]^{-1}$ is the integer covariance and $[\hat{\boldsymbol{S}}_k^N]^{-1}\hat{\boldsymbol{y}}_k^N$ is the estimate of the integer vector $\boldsymbol{N}$ at epoch k. Once all n epochs are processed, the resulting satellite cycle ambiguity estimates are substituted into Eq. (51), and a weighted least-squares fit (based on the integer covariance) is used to obtain the trajectory update. The entire process is then repeated until the magnitude of the trajectory update is negligibly small.

For a stack size of $n = 50$, execution time of the reduced-order information smoother algorithm is, typically, 0.5–1 s on a Pentium processor. It is noted again that the increase in execution speed is gained at the expense of not obtaining the actual least-squares solution to Eq. (36); however, the resulting cycle ambiguity error compared with the full least-squares solution is typically less than 0.01 L1 cycles (< 2 mm). As will be discussed shortly, both the iterated information smoother and reduced-order smoother algorithms have been used extensively in real-time flight testing.

Convergence

It is crucial that convergence be guaranteed for an algorithm intended for use in real-time, zero-visibility precision landing operations. For a given pseudolite overflight, the convergence characteristics of the simple Gauss–Newton iteration procedure described in the preceding sections will depend exclusively on the quality of the initial guess trajectory. To assess the limits of convergence of the Gauss–Newton iteration procedure, a computer simulation was developed, which to the maximum extent possible, incorporated the actual real-time flight algorithms. The satellite constellation orbital parameters were obtained from a recent GPS constellation almanac; the satellite orbits were propagated analytically using a straightforward Keplerian orbit model. GPS satellite outages were included in the simulation using the Phlong and Elrod[13] satellite state availability model, which incorporates allowances for both scheduled downtime for satellite maintenance (such as stationkeeping maneuvers) and unscheduled downtime due to satellite system failures.

The simulated navigation system architecture consisted of three pseudolites placed at the instrument landing system (ILS) middle marker site. The corresponding altitude of pseudolite overflight was approximately 200 ft. In addition, a pseudolite bubble radius of 600 ft, a 7.5-deg elevation mask, and a 5-Hz update rate were used. A standard 3-deg glideslope approach at San Francisco International runway 28 was repeatedly simulated in the presence of varying satellite geometry and availability. Finally, the error in the initial guess trajectory was systematically varied with the goal of generating a convergence map for the Gauss–Newton iteration procedure.

Figure 9a shows the region of algorithm convergence with respect to crosstrack and vertical errors in the initial guess trajectory for all satellite geometries. (Also shown are the crosstrack positions of the pseudolites, indicated by the ○ symbols in the figure.) The results are interpreted as follows. The aircraft position during the approach (indicated by the + symbol) is perfect; there are no deviations from the nominal approach path. However, the aircraft's knowledge of its crosstrack and vertical position components can be in error; the size of this error is specified by the assumed aircraft position given by the horizontal and vertical axes in the figure. For comparison, the approximate navigation sensor error (NSE) of code-based DGPS, the actual source of the initial guess trajectory, is also indicated in the figure. Clearly, even extremely rare code DGPS errors of large magnitude lie well within the computed crosstrack–vertical convergence boundary. A similarly large convergence margin for intrack DGPS errors (not shown) was also obtained from the simulation.

In practice, of course, it is improbable that the aircraft will fly precisely between the pseudolites at the nominal altitude. To ensure

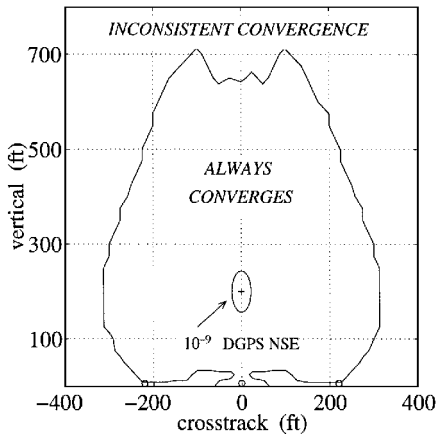

a) Nominal approach

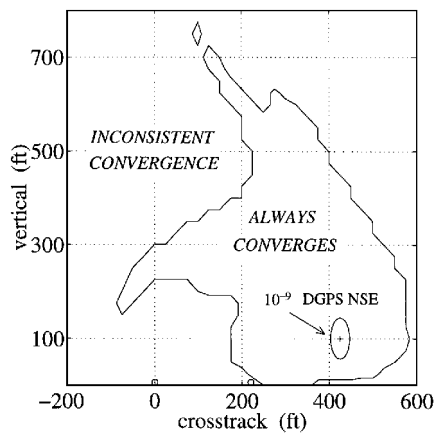

b) Limit-case approach

Fig. 9 Convergence map.

a safe approach and landing, however, the aircraft total system error, the actual deviation from the nominal flight path, must not be too large. For example, at a nominal altitude of 200 ft, one proposed outer containment surface boundary for a GPS-based approach has a half-width and half-height of roughly 400 and 100 ft, respectively.[14] A breach of this containment surface is permitted to occur in only 1 out of 10^7 approaches. Therefore, to bound the convergence performance of the Gauss–Newton iteration procedure, the described simulation was repeated with the actual aircraft position coincident with the containment surface boundary. The result obtained from simulation for the worst-case aircraft offset is shown in Fig. 9b, in which the actual aircraft position deviates from nominal by 400 ft in crosstrack and is also 100 ft below nominal altitude. The simulation results show that, even in this limiting case, a large convergence margin is still present.

Flight-Test Verification

The performance of the real-time information smoothing algorithms has been investigated through extensive flight testing. This section provides the results of two of these flight experiments.

Piper Dakota Approach

The first series of flight tests were performed on a Piper Dakota at Palo Alto Airport in January 1993. Because a datalink was not present in these initial tests, data were stored onboard the aircraft and at the reference station for postprocessing. The purpose of these initial flight trials was simply to verify the overall concept and the prototype carrier phase processing algorithms.

With this goal in mind, the flight experiments were carried out with two ground-based pseudolites placed under the approach path, such that the altitude at pseudolite overflight was approximately 100 m. The ratio of the pseudolite signal low-power radius to the ra-

dius of closest aircraft approach was approximately 3:1 for both pseudolites. Six-channel TANS receivers were used both in the aircraft and on the ground. During the pseudolite overflight, four channels on each of receivers (reference and airborne) were used to track satellites, and the remaining two channels were dedicated to tracking the two pseudolites. Two TANS patch antennas were mounted on the aircraft fuselage (one on the top and one on the belly). The pseudolite and spacecraft carrier phase measurements were collected and stored at a rate of 1 Hz at the aircraft and ground station. In addition, the aircraft attitude was obtained from an independent onboard GPS-based attitude system[15] and was also stored to allow for postflight computation of the moment arm corrections [Eqs. (28) and (29)]. After the last approach and landing, the aircraft taxied to its tiedown position, at which point an independent static GPS survey of the baseline from the reference station antenna to the aircraft antenna was performed. This baseline provided a source of truth for the aircraft position at tiedown accurate to approximately 1 cm and, thereby, provided the means for independent verification of cycle ambiguities for the last approach.

The data collected during pseudolite overflight were postprocessed in the laboratory using the iterated information smoother algorithm. The guess trajectory used to initialize the Gauss–Newton iteration procedure was obtained using code-based DGPS position fixes, which were also stored aboard the aircraft during flight. No prior knowledge of the cycle ambiguities was assumed in the processing of the carrier phase data.

The cycle ambiguity estimation results for a typical approach are shown in Fig. 10 for an arbitrary satellite (PRN 15). Figure 10 shows the integer (cycle ambiguity) estimate error and estimate error covariance history generated during the final forward sweep of the information filter. In a rather straightforward way, Fig. 10 illustrates, through experimental means, both the observability for direct cycle ambiguity resolution using ground-based pseudolites and the typical performance of the cycle ambiguity estimation algorithm. After only three measurement epochs, the system is overdetermined and integer estimates are available. After eight epochs, the integer for SV 15 is known with a standard deviation of five L1 cycles. Finally, at bubble exit, the integer error standard deviation is 0.1 cycles and the actual integer error is 0.01 cycles. The error in the resulting postbubble position fixes was inferred by the independent survey at tiedown to be less than 2 cm.

Boeing 737 Automatic Landings

The cycle ambiguity resolution algorithms were also ultimately tested within the context of their actual intended application: providing reliable real-time navigation output for aircraft automatic landing. Under FAA sponsorship, a United Airlines Boeing 737-300 was equipped with the breadboard differential carrier system to verify its capability to provide the aircraft autopilot with navigation input suitable for automatic landing. The flight tests were carried out in October 1994 at the NASA Ames Crows Landing flight test facility in central California.

Two Aeronautical Radio Inc. 743 GPS antennas were mounted on the aircraft fuselage (one on the top and one on the belly). Additional minor modifications were necessary in the airborne system to provide the aircraft autopilot with an analog GPS navigation output that emulated the nominal ILS glideslope and localizer signal.[16] Real-time aircraft attitude for the two-antenna moment arm correction was obtained from one of the 737's two onboard inertial units.

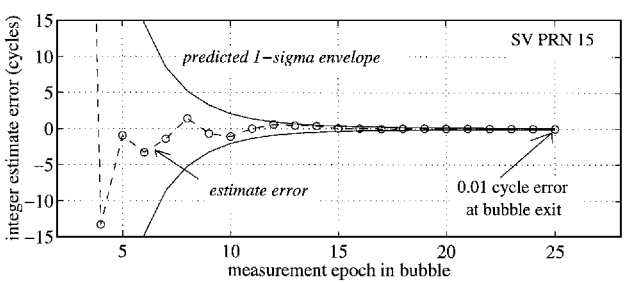

Fig. 10 Piper Dakota pseudolite overflight.

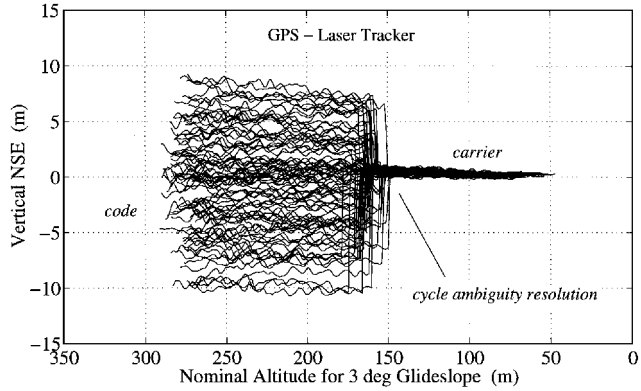

Fig. 11 GPS-laser vertical position differences for Boeing 737 autolands.

On the ground, two pseudolites were situated under the approach path 3.5 km from the runway threshold, corresponding to a pseudolite overflight altitude of 600 ft. As was the case in earlier flight tests, the ratio of pseudolite bubble radius to the radius of closest approach was set to approximately 3:1 for both pseudolites. A reference station very high-frequency datalink update rate of 2 Hz was used; this provided the aircraft with 40–50 measurement epochs for cycle ambiguity resolution during a typical pseudolite overflight. Six-channel TANS receivers were used both in the aircraft and on the ground.

An NdYAG laser tracker at Crows Landing provided range, azimuth, and elevation to a retroreflector mounted on the 737 nose landing gear and was used to obtain the true aircraft position history during each approach. In actuality, the specified laser range accuracy of ± 1 ft (1σ) and elevation and azimuth accuracy of ± 0.2 mrad (1σ) provided reference position fixes considerably less accurate than the expected centimeter-level performance of the test system.

In total, 111 approaches were executed over three days of flight tests. Because only four of the six channels of TANS airborne and ground receivers were allocated for satellite tracking (the remaining two channels were dedicated to tracking the pseudolites), the resulting usable satellite geometries were relatively poor throughout the testing. The effect of this condition, although present during the entirety of each approach, was most notable in positioning prior to pseudolite overflight, where code-based DGPS was employed. During this phase of flight, the resulting vertical positioning error was conspicuously larger than that actually achievable using a state-of-the-art code DGPS architecture, in which at least seven channels would typically be allocated to satellite tracking. In this case, the typical performance is on the order of 1–2 m (95% vertical error).

The vertical NSE history, as measured by the laser tracker, for 95 representative approaches is shown in Fig. 11. On each of these approaches, cycle ambiguity resolution was successfully accomplished within approximately 1 s after bubble exit using the real-time reduced-order algorithm. The exceptional improvement in accuracy exhibited after cycle ambiguity resolution, resulting from the transition to kinematic carrier phase positioning, is clearly evident in the plot. The measured 95% vertical error (ensemble of all of the approaches) after cycle ambiguity resolution was 0.2 m, substantially better than the existing ILS vertical accuracy specification of 0.6 m. Furthermore, this error statistic agreed quite well with the laser tracker error specifications listed earlier, lending support to the hypothesis that error of the GPS navigation output during the approach was much smaller than the laser error.

Conclusion

The high-speed nonlinear information smoothing algorithms described have been demonstrated to provide the capability for real-time cycle ambiguity resolution for application to aircraft precision approach and landing. Using a laser tracker as reference, a vertical navigation sensor error of 0.2 m (95%) was established during an extensive battery of flight tests performed on a Boeing 737.

Appendix: Adding and Removing States

Adding a Satellite or Pseudolite

The principle behind adding a new satellite or pseudolite is exceedingly simple in the information smoother. If a new ranging source is acquired by the receivers between measurement epochs k and $k+1$ and no prior knowledge of the new cycle ambiguity is assumed, the new unknown cycle ambiguity state is appended at the end of the state vector, and the information matrix for epoch k is simply appended with zeros as follows:

$$\hat{\boldsymbol{P}}_k^{\text{new}} = \lim_{\mu \to \infty} \begin{bmatrix} \hat{\boldsymbol{P}}_k^{\text{old}} & \mathbf{0} \\ \mathbf{0} & \mu \end{bmatrix} \quad \Rightarrow \quad \hat{\boldsymbol{S}}_k^{\text{new}} = \begin{bmatrix} \hat{\boldsymbol{S}}_k^{\text{old}} & \mathbf{0} \\ \mathbf{0} & 0 \end{bmatrix} \tag{A1}$$

Similarly, the information vector consistent with Eq. (A1) is then

$$\hat{\boldsymbol{y}}_k^{\text{new}} = \begin{bmatrix} \hat{\boldsymbol{y}}_k^{\text{old}} \\ 0 \end{bmatrix} \tag{A2}$$

This process can be repeated as necessary to accommodate the case where more than one new ranging source is acquired between measurement epochs k and $k+1$. The processing of the measurements collected at epoch $k+1$ can now continue in the nominal manner.

Removing a Satellite or Pseudolite

The mechanics of removing a satellite or pseudolite is somewhat more involved in that matrix partitioning and block inversion is necessary. Consider first the case where the last cycle ambiguity state is to be removed from the state vector before processing of epoch $k+1$. In this case, the last column and row of the covariance matrix for epoch k must be deleted. Using the definition of the information matrix expressed in block partitioned form, we can write

$$\hat{\boldsymbol{P}}_k^{\text{old}} = \begin{bmatrix} \hat{\boldsymbol{P}}_k^{\text{new}} & \bullet \\ \bullet & \bullet \end{bmatrix} = \begin{bmatrix} \hat{\boldsymbol{S}}_k^{1} & \hat{\boldsymbol{S}}_k^{12} \\ \hat{\boldsymbol{S}}_k^{12^{\top}} & \hat{s}_k^{2} \end{bmatrix}_{\text{old}}^{-1} \tag{A3}$$

where $\hat{s}_k^2$ is a nonzero scalar. Applying the matrix block inversion identity, we obtain

$$\hat{\boldsymbol{S}}_k^{\text{new}} = \left[\hat{\boldsymbol{P}}_k^{\text{new}}\right]^{-1} = \left[\hat{\boldsymbol{S}}_k^{1} - \hat{\boldsymbol{S}}_k^{12}\hat{\boldsymbol{S}}_k^{12^{\top}} \big/ \hat{s}_k^{2}\right]_{\text{old}} \tag{A4}$$

An analogous procedure for the information vector produces

$$\hat{\boldsymbol{y}}_k^{\text{new}} = \left[\hat{\boldsymbol{y}}_k^{1} - \hat{\boldsymbol{S}}_k^{12}\hat{y}_k^{2} \big/ \hat{s}_k^{2}\right]_{\text{old}} \tag{A5}$$

The case where an arbitrary satellite i (not necessarily the one corresponding to the last cycle ambiguity state) is to be deleted is handled as follows. Remove the ith row and column of the information matrix and ith element of the information vector; the remaining matrix and vector are defined to be $\hat{\boldsymbol{S}}_k^1$ and $\hat{\boldsymbol{y}}_k^1$, respectively. Element (i, i) of the information matrix is defined to be $\hat{s}_k^2$, and element i of the information vector is defined to be $\hat{y}_k^2$. Finally, $\hat{\boldsymbol{S}}_k^{12}$ is defined to be column i of the information matrix with element (i, i) removed. Using these definitions, Eqs. (A4) and (A5) can be applied directly to obtain the new information matrix and vector.

Acknowledgments

The authors gratefully acknowledge the Federal Aviation Administration for supporting this research. The contributions of Clark E. Cohen, David G. Lawrence, and H. Stewart Cobb are greatly appreciated.

References

[1] Counselman, C. C., and Shapiro, I. I., "Miniature Interferometer Terminals for Earth Surveying," *Bulletin Geodesique*, Vol. 53, No. 2, 1979, pp. 139–163.

[2] MacDoran, P., "Satellite Emission Radio Interferometric Earth Surveying (SERIES)—GPS Geodetic System," *Bulletin Geodesique*, Vol. 53, No. 2, 1979, pp. 117–138.

[3] Remondi, B. W., "Performing Centimeter-Level Surveys in Seconds with GPS Carrier Phase: Initial Results," *Navigation*, Vol. 32, No. 4, Winter 1985–1986.

[4] Hatch, R. R., "Instantaneous Ambiguity Resolution," *Proceedings of the International Association of Geodesy Symposium No. 107 on Kinematic Systems in Geodesy, Surveying and Remote Sensing*, Banff, Canada, Sept. 1990.

[5] Hatch, R. R., and Euler, H.-J., "Comparison of Several AROF Kinematic Techniques," *Proceedings of the Seventh International Technical Meeting of the Satellite Division of the Institute of Navigation (ION GPS-94)* (Salt Lake City, UT), Inst. of Navigation, 1994.

[6] Klein, D., and Parkinson, B. W., "The Use of Pseudo-Satellites for Improving GPS Performance," *Navigation*, Vol. 31, No. 4, Winter 1984–1985.

[7] Parkinson, B. W., and Fitzgibbon, K. T., "Aircraft Automatic Landing Systems Using GPS," *Journal of Navigation*, Vol. 42, No. 1, 1989.

[8] Cohen, C. E., Pervan, B. S., Cobb, H. S., Lawrence, D. G., Powell, J. D., and Parkinson, B. W., "Real-Time Cycle Ambiguity Resolution Using a Pseudolite for Precision Landing of Aircraft with GPS," *Proceedings of the Second International Conference on Differential Satellite Navigation Systems (DSNS-93)*, Amsterdam, March–April 1993.

[9] Pervan, B. S., "Navigation Integrity for Aircraft Precision Landing Using the Global Positioning System," Ph.D. Dissertation, Dept. of Aeronautics and Astronautics, Stanford Univ., Stanford, CA, March 1996.

[10] Lawrence, D. G., Pervan, B. S., Cohen, C. E., Cobb, H. S., Powell, J. D., and Parkinson, B. W., "Real-Time Architecture for Kinematic GPS Applied to the Integrity Beacon Landing System," *Proceedings of the 51st Annual Meeting* (Colorado Springs, CO), Inst. of Navigation, 1995.

[11] Van Graas, F., and Lee, S.-W., "High-Accuracy Differential Positioning for Satellite-Based Systems Without Using Code-Phase Measurements," *Proceedings of the Institute of Navigation National Technical Meeting* (Anaheim, CA), Inst. of Navigation, 1995.

[12] Bryson, A. E., and Ho, Y. C., *Applied Optimal Control*, Hemisphere, New York, 1975.

[13] Phlong, W. S., and Elrod, B. D., "Availability Characteristics of GPS and Augmentation Alternatives," *Navigation*, Vol. 40, No. 4, Winter 1993–1994.

[14] Kelly, R. J., and Davis, J. M., "Required Navigation Performance (RNP) for Precision Approach and Landing with GNSS Application," *Navigation*, Vol. 41, No. 1, Spring 1994.

[15] Cohen, C. E., "Attitude Determination Using GPS," Ph.D. Dissertation, Dept. of Aeronautics and Astronautics, Stanford Univ., Stanford, CA, Dec. 1992.

[16] Cohen, C. E., Cobb, H. S., Lawrence, D. G., Pervan, B. S., Barrows, A. K., O'Connor, M. L., Gromov, K. G., Elkaim, G. H., Christie, J., Powell, J. D., Parkinson, B. W., Aubrey, G. J., Loewe, W., Ormiston, D., McNally, B. D., Kaufmann, D. N., Wullschleger, V., and Swider, R., "Automatic Landing of a 737 Using GNSS Integrity Beacons," *Proceedings of the International Symposium on Precision Approach and Landing (ISPA 95)*, Braunschweig, Germany, Feb. 1995.